

This figure "irwinj.ap01.N1421-pg1.jpg" is available in "jpg" format from:

<http://arxiv.org/ps/astro-ph/9811351v1>

This figure "irwinj.ap03.N2613-pg1.jpg" is available in "jpg" format from:

<http://arxiv.org/ps/astro-ph/9811351v1>

This figure "irwinj.ap04.N2683-pg1.jpg" is available in "jpg" format from:

<http://arxiv.org/ps/astro-ph/9811351v1>

This figure "irwinj.ap05.I0564-pg1.jpg" is available in "jpg" format from:

<http://arxiv.org/ps/astro-ph/9811351v1>

This figure "irwinj.ap06.N3044-pg1.jpg" is available in "jpg" format from:

<http://arxiv.org/ps/astro-ph/9811351v1>

This figure "irwinj.ap08.N3221-pg1.jpg" is available in "jpg" format from:

<http://arxiv.org/ps/astro-ph/9811351v1>

This figure "irwinj.ap09.N3432-pg1.jpg" is available in "jpg" format from:

<http://arxiv.org/ps/astro-ph/9811351v1>

This figure "irwinj.ap10.N3556-pg1.jpg" is available in "jpg" format from:

<http://arxiv.org/ps/astro-ph/9811351v1>

This figure "irwinj.ap12.N3735-pg1.jpg" is available in "jpg" format from:

<http://arxiv.org/ps/astro-ph/9811351v1>

This figure "irwinj.ap13.N4157-pg1.jpg" is available in "jpg" format from:

<http://arxiv.org/ps/astro-ph/9811351v1>

This figure "irwinj.ap14.N4388-pg1.jpg" is available in "jpg" format from:

<http://arxiv.org/ps/astro-ph/9811351v1>

This figure "irwinj.ap16.N4517-pg1.jpg" is available in "jpg" format from:

<http://arxiv.org/ps/astro-ph/9811351v1>

This figure "irwinj.ap17.N4746-pg1.jpg" is available in "jpg" format from:

<http://arxiv.org/ps/astro-ph/9811351v1>

This figure "irwinj.ap18.N5297-pg1.jpg" is available in "jpg" format from:

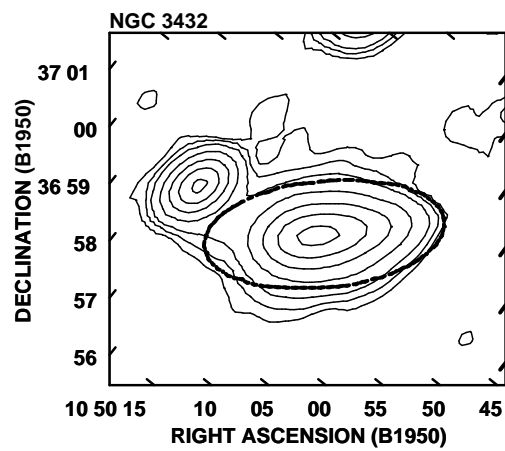
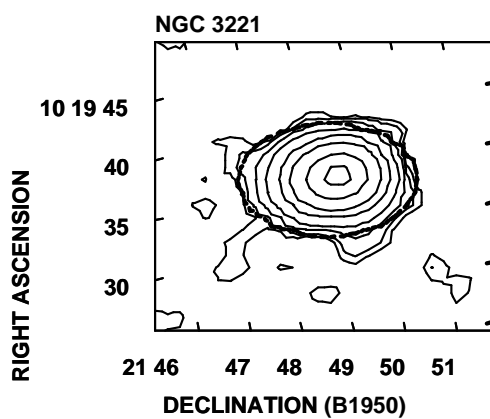
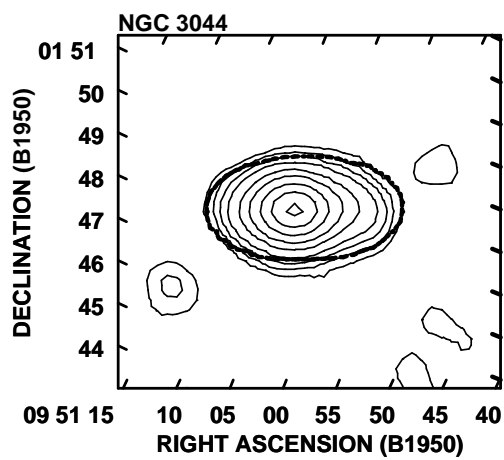
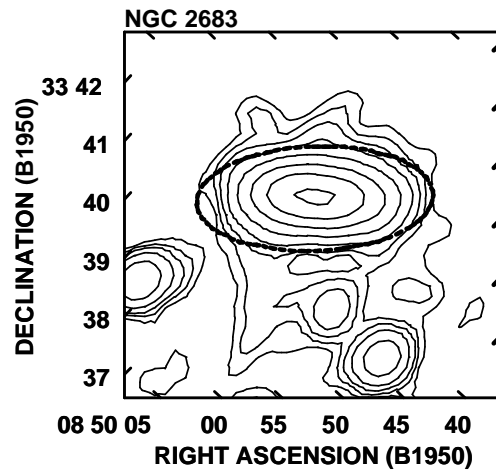
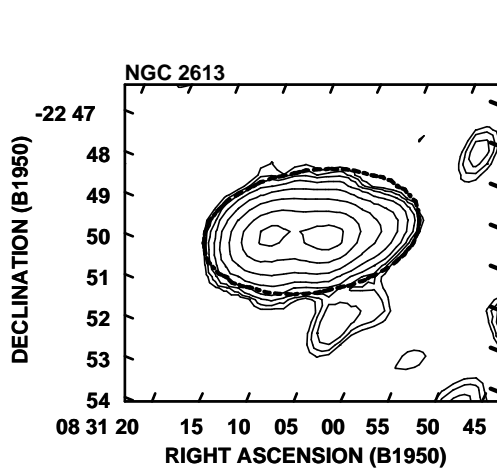
<http://arxiv.org/ps/astro-ph/9811351v1>

This figure "irwinj.ap19.N5433-pg1.jpg" is available in "jpg" format from:

<http://arxiv.org/ps/astro-ph/9811351v1>

This figure "irwinj.ap20.N5775-pg1.jpg" is available in "jpg" format from:

<http://arxiv.org/ps/astro-ph/9811351v1>



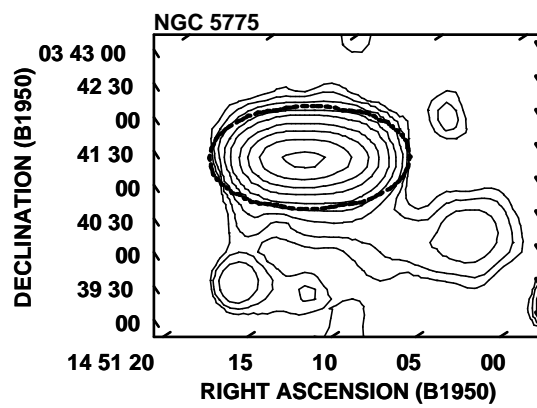
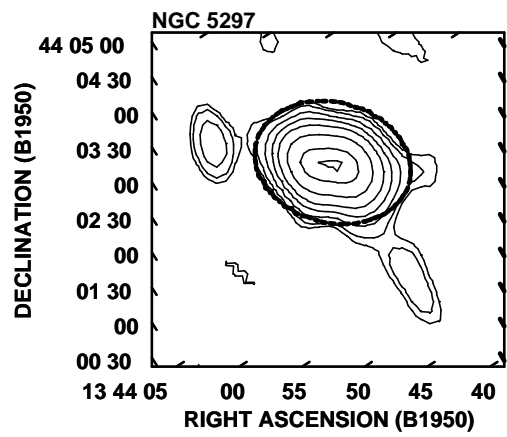
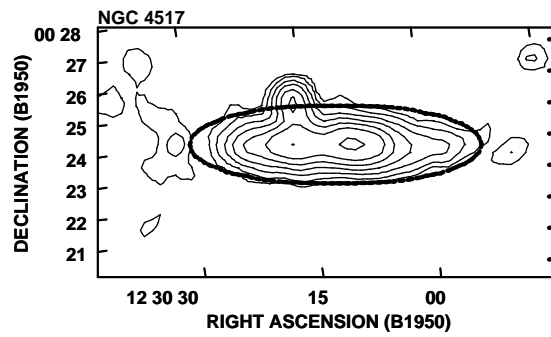
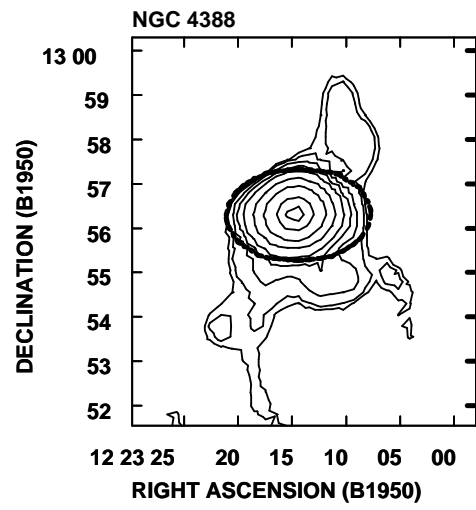
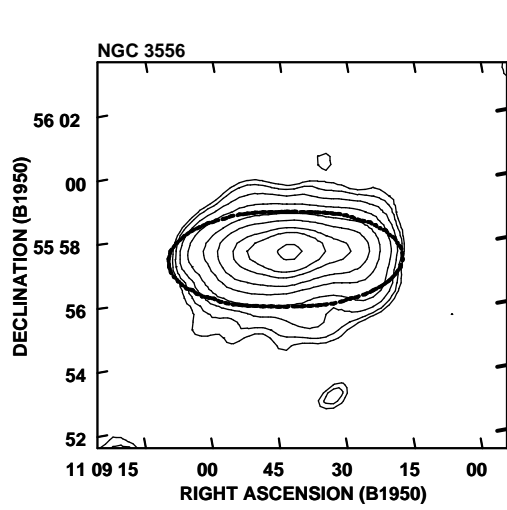


TABLE 1. The Galaxy Sample and Some Basic Properties.

Name	Velocity 3°K km s ⁻¹	Distance Mpc	P.A. deg	Optical Axes		Inclination	
				Major arcmin	Minor arcmin	Max. deg	Min. deg
(1)	(2)	(3)	(4)	(5)	(6)	(7)	(8)
NGC 1421	1958	26.1	0	3.5	0.9	90	76
NGC 2613	1940	25.9	113	7.2	1.8	85	76
NGC 2683	626	8.4	44	9.3	2.2	79	76
IC 0564	6354	84.7	68	1.7	0.4	84	75
NGC 3044	1627	21.7	113	4.9	0.7	90	82
NGC 3221	4415	58.9	167	3.2	0.7	90	78
NGC 3432	880	11.7	38	6.8	1.5	82	77
NGC 3556	866	11.6	80	8.7	2.2	84	75
NGC 3735	2780	37.1	131	4.2	0.8	85	79
NGC 4157	969	12.9	66	6.8	1.3	90	79
NGC 4388	2843	20.0	92	5.6	1.3	79	77
NGC 4517	1460	19.5	83	10.5	1.5	90	82
NGC 4746	2093	27.9	120	3.8	1.1	80	72
NGC 5297	2590	34.5	148	5.6	1.3	89	77
NGC 5433	4557	60.8	3	1.6	0.4	85	76
NGC 5775	1886	25.2	146	4.2	1.0	84	76

Notes to Table 1.

Column (2) is the recessional velocity relative to the 3°K background from de Vaucouleurs et al. (1991), hereafter the RC3; (3) is the distance computed using column (2) values and $H_0 = 75 \text{ km s}^{-1} \text{ Mpc}^{-1}$ except for NGC 4388 which is believed to be in the Virgo Cluster (Phillips & Malin 1982) (4) is the position angle and (5) and (6) are optical angular diameters. The maximum inclination (7) is taken from Tully (1988) or (in the case of emphasized values) calculated according to the formula given in Tully (1988) which assumes a thick disk ($c/a=0.2$), while the minimum inclination (8) assumes a thin disk ($\cos i = b/a$).

TABLE A1. Contour Levels for 20 cm C-array Maps

Galaxy	Uniform Weighting (mJy beam ⁻¹)	Natural Weighting (mJy beam ⁻¹)
NGC 1421	0.216 × (1, 2, 5, 10, 15, 20, 30, 40, 50, 60, 70)	0.187 × (1, 2, 5, 10, 15, 20, 30, 40, 50, 60, 70)
NGC 2613	0.153 × (1, 2, 4, 6, 8, 10, 12, 14, 16, 18, 20, 22, 24, 26, 28, 30)	0.134 × (1, 2, 4, 6, 8, 10, 12, 14, 16, 18, 20, 22, 24, 26, 28, 30)
NGC 2683	0.129 × (1, 2, 3, 5, 7, 10, 13, 16, 20, 25, 30)	0.159 × (1, 2, 3, 5, 7, 10, 13, 16, 20, 25, 30)
IC 0564	0.231 × (1, 2, 5, 7, 10, 15, 25, 35, 45, 55, 65, 75)	0.172 × (1, 2, 5, 10, 15, 30, 45, 60, 75, 90, 100)
NGC 3044	0.163 × (1, 2, 3, 5, 7, 10, 15, 20, 30, 40, 50, 60, 80, 100, 120)	0.186 × (1, 2, 3, 5, 7, 10, 15, 20, 30, 40, 50, 60, 80, 100, 120, 140, 150)
NGC 3221	0.249 × (1, 2, 5, 10, 20, 30, 40, 50, 60, 70, 80, 90, 100)	0.276 × (1, 2, 5, 10, 20, 30, 40, 50, 60, 70, 80, 90, 100)
NGC 3432	0.092 × (1, 2, 3, 5, 7, 10, 15, 20, 30, 40, 60, 80, 100, 120, 140, 160, 180, 200)	0.095 × (1, 1, 2, 3, 5, 7, 10, 15, 20, 30, 40, 60, 80, 100, 120, 140, 160, 180, 200)
NGC 3556	0.11 × (1, 2, 3, 5, 7, 10, 15, 20, 30, 40, 50, 60, 70, 80, 100, 125, 150)	0.086 × (1, 1, 2, 3, 5, 7, 10, 15, 20, 30, 40, 50, 60, 70, 80, 100, 125, 150, 175, 200, 225, 250, 275, 300)
NGC 3735	0.271 × (1, 2, 3, 5, 10, 15, 20, 30, 40, 50, 60, 80, 100)	0.262 × (1, 2, 3, 5, 7, 10, 15, 20, 30, 40, 50, 60, 80, 100, 120, 140)
NGC 4157	0.224 × (1, 2, 3, 5, 7, 10, 15, 20, 30, 40, 60, 80, 100, 120, 140, 160, 180, 200)	0.198 × (1, 2, 3, 5, 7, 10, 15, 20, 30, 40, 60, 80, 100, 120, 140, 160, 180, 200)
NGC 4388	0.402 × (1, 2, 5, 10, 15, 25, 50, 75, 100, 120)	0.46 × (1, 2, 5, 10, 15, 25, 50, 75, 100, 120)
NGC 4517	0.088 × (1, 2, 4, 6, 8, 10, 15, 20, 25, 30, 35, 40)	0.089 × (1, 2, 4, 6, 8, 10, 15, 20, 25, 30, 35, 40)
NGC 4746	0.165 × (1, 2, 3, 5, 7, 10, 15, 20, 25, 30, 35, 40)	0.162 × (1, 2, 3, 5, 7, 10, 15, 20, 30, 40, 50, 60, 70, 80, 85, 90)
NGC 5297	0.125 × (1, 2, 3, 4, 5, 6, 7, 8, 9, 10, 11, 12, 13, 14, 15)	0.116 × (1, 2, 3, 4, 5, 6, 7, 8, 9, 10, 11, 12, 13, 14, 15)
NGC 5433	0.229 × (1, 2, 3, 5, 7, 10, 20, 40, 60, 80, 100, 120, 140, 160)	0.265 × (1, 2, 3, 5, 7, 10, 20, 40, 60, 80, 100, 120, 140, 160)
NGC 5775	0.182 × (1, 2, 3, 5, 7, 10, 15, 20, 40, 60, 80, 100, 120)	0.184 × (2, 3, 5, 7, 10, 20, 40, 60, 80, 100, 120)

This figure "irwinj.ap02.N1421-pg2.jpg" is available in "jpg" format from:

<http://arxiv.org/ps/astro-ph/9811351v1>

This figure "irwinj.ap07.N3044-pg2.jpg" is available in "jpg" format from:

<http://arxiv.org/ps/astro-ph/9811351v1>

This figure "irwinj.ap11.N3556-pg2.jpg" is available in "jpg" format from:

<http://arxiv.org/ps/astro-ph/9811351v1>

This figure "irwinj.ap15.N4388-pg2.jpg" is available in "jpg" format from:

<http://arxiv.org/ps/astro-ph/9811351v1>

This figure "irwinj.ap21.N5775-pg2.jpg" is available in "jpg" format from:

<http://arxiv.org/ps/astro-ph/9811351v1>

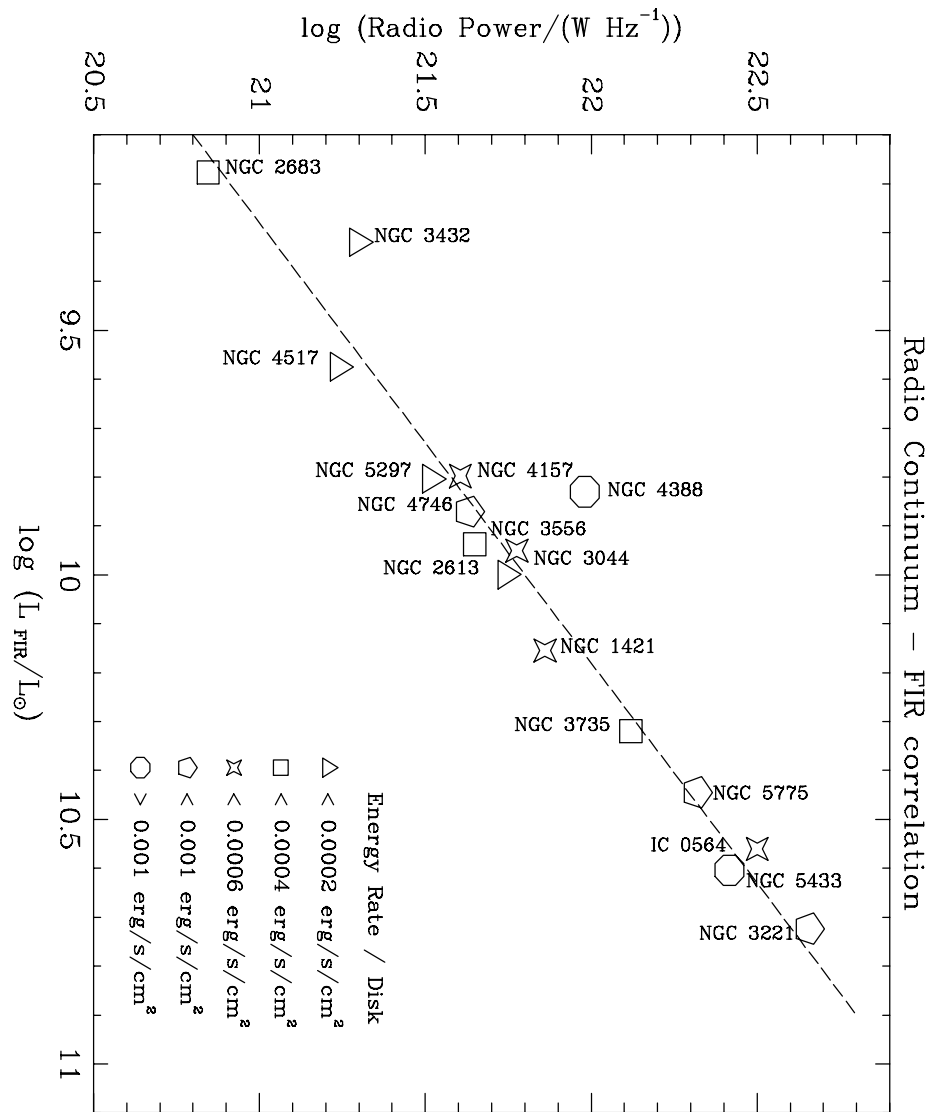


TABLE 2. Observing and Map Parameters

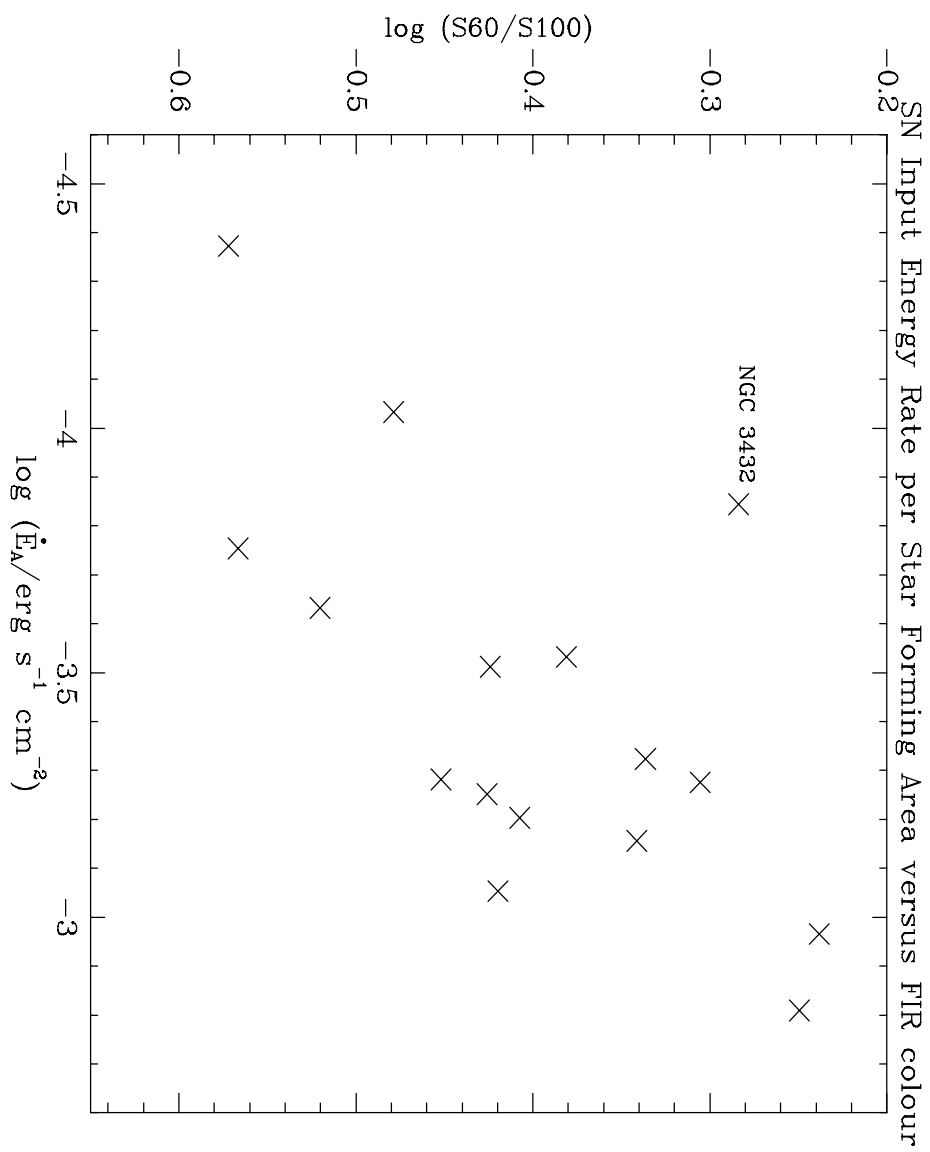
Name (1)	Scale kpc arcsec ⁻¹ (2)	r.m.s. μ Jy (3)	C Array Observations			20 cm		D Array Observations			r.m.s. μ Jy (11)	D ma a
			major axis arcsec (4)	minor axis arcsec (5)	p.a. deg (6)	r.m.s. μ Jy (7)		major axis arcsec (8)	minor axis arcsec (9)	p.a. deg (10)		
NGC 1421	0.127	108	14.5	12.3	-28	336		118.8	36.0	44	90	
		94	17.6	13.6	-25	232		181.0	38.7	47	58	
NGC 2613	0.125	76	18.4	11.1	-16	166		66.5	40.3	-8	-	
		67	23.0	13.0	-15	123		83.9	48.9	-7	-	
NGC 2683	0.041	65	17.4	13.5	-70	84		46.7	40.8	-57	-	
		80	27.4	17.5	-66	151		60.8	50.2	-83	-	
IC 0564	0.411	116	16.0	15.0	-52	-		-	-	-	-	
		86	17.8	15.7	-22	-		-	-	-	-	
NGC 3044	0.105	81	12.0	11.9	-44	101		48.7	47.0	-53	58	
		93	18.9	15.9	-7	100		55.6	55.2	43	46	
NGC 3221	0.285	125	11.5	11.3	-40	191		38.3	37.1	33	-	
		138	15.6	14.9	-22	250		51.3	49.3	-34	-	
NGC 3432	0.057	46	13.2	12.8	51	96		55.3	38.4	85	-	
		48	16.9	15.9	-67	109		80.8	50.9	73	-	
NGC 3556	0.056	55	22.7	12.3	-72	99		50.3	49.5	-46	75	
		43	32.8	19.0	-66	180		61.5	53.8	-61	46	
NGC 3735	0.180	135	34.3	20.5	-51	-		-	-	-	-	
		131	41.2	30.1	-49	-		-	-	-	-	
NGC 4157	0.063	112	21.1	11.3	-81	-		-	-	-	-	
		99	27.9	15.5	-75	-		-	-	-	-	
NGC 4388	0.097	201	12.7	12.1	11	367		38.3	37.2	-35	64	
		230	17.5	14.7	-7	1350		52.9	47.6	-1	52	
NGC 4517	0.094	44	15.4	13.7	-62	108		46.4	43.7	-51	-	
		44	18.9	16.4	-17	106		54.4	46.7	1	-	
NGC 4746	0.135	83	12.6	11.9	-25	-		-	-	-	-	
		81	17.7	14.9	1	-		-	-	-	-	
NGC 5297	0.167	63	12.3	11.2	-25	138		64.5	36.6	83	-	
		58	15.9	15.4	-36	128		88.7	48.1	74	-	
NGC 5433	0.295	114	11.6	11.5	-43	-		-	-	-	-	
		132	16.0	15.6	-28	-		-	-	-	-	
NGC 5775	0.122	91	15.2	14.1	-56	92		45.2	44.4	-89	57	
		92	18.0	15.8	-25	86		52.0	51.4	44	70	

Notes to Table 2.

The scale for each image (2) is calculated using the distance in Table 1. For each galaxy we list the r.m.s. noise, major and minor axis as well as beam position angle. The values in the first line correspond to uniform weighting and the second line corresponds to natural weighting reduction details. Beams are also plotted on the images in Appendix A.

TABLE A2. Contour Levels for 20 cm D-array Maps

Galaxy	Levels (mJy beam^{-1})
NGC 2613	$0.246 \times (1, 2, 3, 5, 7, 10, 15, 20, 25, 30, 35, 40, 45, 50, 55, 60)$
NGC 2683	$0.30 \times (1.0, 1.7, 2.5, 4.1, 8.3, 16.6, 30, 50)$
NGC 3044	$0.20 \times (1, 2.5, 5, 10, 25, 50, 100, 175, 275)$
NGC 3221	$0.50 \times (1, 1.6, 3, 6, 15, 30, 70, 120)$
NGC 3432	$0.22 \times (1, 2.3, 4.5, 13.6, 34, 68, 114)$
NGC 3556	$0.36 \times (1, 2, 3, 5, 7, 10, 15, 20, 30, 40, 50, 60, 80, 100, 120, 140, 160, 180, 200)$
NGC 4388	$2.5 \times (1, 1.2, 1.8, 2.6, 4, 8, 16, 32, 44)$
NGC 4517	$0.20 \times (1, 2, 3.75, 6.25, 10, 15, 25)$
NGC 5297	$0.24 \times (1, 1.7, 3.1, 5.2, 8.3, 14.6, 25, 31.3)$
NGC 5775	$0.172 \times (1, 2, 5, 10, 20, 40, 60, 80, 100, 150, 200, 250, 300, 350, 400, 450, 500, 550, 600)$



High Latitude Radio Emission in a Sample of Edge-On Spiral Galaxies

Judith A. Irwin

irwin@astro.queensu.ca

Jayanne English

english@astro.queensu.ca

and

Barkat Sorathia¹

sorathia@polaris.phys.yorku.ca

Queen's University

Dept. of Physics

Kingston, Ontario, Canada, K7L 3N6

Received _____; accepted _____

Submitted to A.J.

¹Now at York University, Physics & Astronomy Dept., 4700 Keele Street, North York, Ontario, Canada, M3J 1P3

ABSTRACT

We have mapped 16 edge-on galaxies at 20 cm using the VLA in its C configuration, and a subset of these galaxies in D configuration at 6 and/or 20 cm in a search for extended ($\gtrsim 1$ kpc) radio continuum emission above and below the plane. For 5 galaxies, we could form spectral index, energy and magnetic field maps (assuming minimum energy). While the galaxies were partly chosen by radio flux density, they span a variety of star formation rates and only 6 might be considered “starburst” galaxies. A range of Hubble type and degree of isolation are also represented. The galaxies largely fall on the FIR-radio continuum correlation. They also display a correlation between IR surface brightness and warmth, extending the previously observed relation of Lehnert & Heckman (1996b) to galaxies with lower star formation rates.

We find that all but one galaxy show evidence for non-thermal high latitude radio continuum emission, suggesting that cosmic ray halos are common in star forming galaxies. Of these, eight galaxies are new detections. The high latitude emission is seen over a variety of spatial scales and in discrete and/or smooth features. In some cases, discrete features are seen on large scales, suggesting that smooth radio halos may consist, in part, of discrete features combined with low spatial resolution. In general, the discrete features emanate from the disk, but estimates of CR diffusion lengths suggest that diffusion alone is insufficient to transport the particles to the high latitudes seen (> 15 kpc in one case). Thus CRs likely diffuse through low density regions and/or are assisted by other mechanisms (e.g. winds).

We searched for correlations between the prevalence of high latitude radio emission and a number of other properties, including the global SFR, supernova input rate per unit star forming area, \dot{E}_A , and environment, and do not find

clear correlations with any of these properties. A subset of the data allow, at best, for only a weak correlation with \dot{E}_A . Our one non-detection (NGC 4517), however, occurs at a threshold level consistent with that found by Dahlem et al. (1995) The lack of a good correlation with star formation indicators could be the result of the different timescales for star formation processes compared to the duration of the radio emission. Correlations with other properties, such as environment, are more difficult to assess. However, a few isolated galaxies display strong radio halos, indicating that an interaction is not necessary to produce the extra-planar emission.

Subject headings: cosmic rays — galaxies:halos — galaxies:spiral — radio continuum

1. Introduction

There is now considerable evidence for galactic halos, thick disks, and discrete connecting features between the disk and halo in many star-forming spiral galaxies. Such features are best detected directly by observing edge-on galaxies with sufficient sensitivity and spatial resolution. High latitude (i.e. $\gtrsim 1$ kpc) emission has now been observed in every ISM tracer (though not necessarily in all tracers in the same galaxy) for example, CO (Irwin & Sofue 1996), IR emission from dust (Howk & Savage 1997), HI (Lee & Irwin 1997), diffuse ionized gas (Rand et al. 1990; Dettmar 1990), X-ray emission from the hot ionized medium (Vogler & Pietsch 1996), and radio synchrotron emission from cosmic rays (CRs) (English & Irwin 1997). For a more complete list, see Dahlem (1997).

To account for emission in galactic halos, several models have been developed which include some form of gas ejection from the disk to the halo, with subsequent infall (circulation or “fountains”) or ejection into the intergalactic medium (Shapiro & Field 1976; Bregman 1980; Norman & Ikeuchi 1989; Heckman et al. 1990; Völk 1991). Processes related to massive star formation (e.g. supernovae, stellar winds) are the focus of these models, although magnetic fields through Parker instabilities (Kamaya et al. 1996), radiation pressure on dust (Franco et al. 1991) and galaxy-galaxy interactions (Golla & Hummel 1994) have also been suggested as playing an important role in some cases. With estimated disk mass-loss rates of $0.3 \rightarrow 3 \text{ M}_{\odot} \text{ yr}^{-1}$ for our own Galaxy (Norman & Ikeuchi 1989) and most likely higher for starbursts (see Heckman et al. 1990; Lehnert & Heckman 1996a; Lehnert & Heckman 1996b) there are important implications for metallicity gradients, the availability of disk gas in an appropriate state for star formation, and indeed for galaxy evolution itself. Faint extended halos, when present, may also trace the more arcane dark matter distributions around galaxies.

Early evidence for high latitude radio features in external spiral galaxies was presented

some years ago by Hummel, van Gorkom, & Kotanyi (1983) who identified 5 edge-on galaxies with discrete radio continuum features apparently associated with nuclear outflow. This prompted one of us (JAI) to initiate a small survey to search for evidence for high latitude radio continuum emission in other edge-on galaxies, whether connected with the underlying disk or nucleus. Since the time of the initial survey, various follow-up observations and radio continuum maps of a few individual galaxies in the sample have been published (see Irwin 1991; Irwin 1995; English & Irwin 1997; Lee & Irwin 1997; King & Irwin 1997 Duric et al. 1998). In this paper, we present the complete survey results (see also Sorathia 1994). For recent reviews of gaseous halos of spiral galaxies see Dettmar (1992) and Dahlem (1997).

2. The Sample

The edge-on galaxies in this sample were chosen from the 1415 MHz Westerbork survey of Hummel (1980; 190 galaxies), supplemented by the 2380 MHz Arecibo survey of Dressel & Condon (1978; 456 galaxies) with declinations high enough for observations at the Very Large Array. A galaxy was considered to be edge-on if its inclination, $i \geq 72^\circ$ ($\log R_{25} \geq 0.52$ as listed in the de Vaucouleurs et al. 1976; hereafter the RC2). We also restricted the sample to galaxies whose total flux densities at 1415 MHz were greater than 50 mJy (> 30 mJy at 2380 MHz) to ensure that they could be mapped in reasonable integration times. Thus, the sample is biased towards galaxies with higher radio flux density, but as we will see in 4.2.1, this does not translate into a bias towards high star formation rate (SFR). A few galaxies of large angular extent were also excluded so as to avoid cases in which halo emission would likely be resolved out in the first data set acquired and also to avoid galaxies which had already been well studied (e.g. M 82). In total, 16 galaxies met the above criteria. These galaxies are listed, along with some of their properties, in Table 1 (we

adopt $H_0 = 75 \text{ km s}^{-1} \text{ Mpc}^{-1}$).

The most extensive radio continuum survey of edge-on spirals carried out to date is that of Hummel et al. 1991 who surveyed 181 galaxies with inclinations $> 75^\circ$ at a frequency of 5 GHz. Most of their galaxies were restricted to optical diameters $< 4'$ and therefore there is only one galaxy, NGC 5775 (UGC 9579), which is common to our respective samples. Hummel et al. detect radio halos in only 5.5% of their galaxies. The main differences between the two surveys are a) we have looked at a smaller radio-selected sample, b) our galaxies are generally of larger angular size and thus we have improved linear resolution, c) with roughly equivalent beam sizes, our sensitivity ranges from a factor of 2 better to a value comparable to that of Hummel et al. (cf. our Table 2 with their Table 3) and d) our observations are at 1.49 GHz, supplemented with some 5 GHz observations (§3), compared to Hummel et al.’s 5 GHz data.

Colbert et al. 1996 have also observed 10 edge-on Seyfert galaxies and 4 non-Seyferts at a frequency of 5 GHz and find that 6 out of 10 Seyferts display extended emission apparently originating at the nucleus. Two of their galaxies, NGC 4388 (a Seyfert) and NGC 3044 are in our sample.

3. Observations and Data Reductions

The first observations were made on 25, 26 July, 1985 at 20 cm (1.49 GHz) using the Very Large Array (VLA) of the National Radio Astronomy Observatory (NRAO) ² in its C configuration. Subsequently, on 27, 28 April 1987 with the VLA in its D configuration, 11 galaxies from the sample were observed at 20 cm and 5 galaxies were observed at 6 cm (5

²The NRAO is operated by Associated Universities Inc., under contract with the National Science Foundation, USA.

GHz). For each observation, the bandwidth was 100 MHz, the primary flux calibrators were 3C48 or 3C286 and nearby phase calibrators were observed every 20 to 30 minutes. The largest angular size visible is 4 arcmin for the C array 20 cm and D array 6 cm observations and 15 arcmin for the D array 20 cm observations. The half-power primary beam size is 30 arcmin at 20 cm and 9 arcmin at 6 cm. On-source integration times were chosen according to prior knowledge of the galaxy’s total flux and ranged from a minimum of 13 minutes to a maximum of 2.8 hours over all observations. The mean on-source time for the C array 20 cm data was 48 minutes, for the D array 20 cm data, the mean was 1.3 hours, and for the D array 6 cm data, the mean was 58 minutes.

For historical reasons, related in part to the way in which the data have been handled over a number of years, we have dealt with each array separately in presenting an overview of the complete survey results. Combined array images have been presented for several individual galaxies elsewhere (see Bloemen et al. 1993; Duric et al. 1998). For each array, then, the UV data were Fourier Transformed into the map plane using both uniform and natural weighting, CLEANed, and self-calibrated (see Perley et al. 1989). The resulting rms noise and synthesized beam parameters are listed in Table 2. The highest linear resolution (cf Columns 2, 4, and 5) ranges from 0.6 to 6.4 kpc, depending on distance. In general, the rms noise is approximately twice the theoretical value for the 20 cm observations (due to background confusing sources and their sidelobes) and is approximately equal to the theoretical value for the 6 cm observations. All maps were then corrected for primary beam attenuation.

4. Results

The intensity maps are displayed in Appendix A. The first is the uniformly weighted C array 20 cm map superposed on an optical image from the Digitized Sky Survey (DSS)³, the second is the naturally weighted C array 20 cm map showing the optical major and minor axes, the third is the naturally weighted D array 20 cm map also showing the optical axes and the fourth is the naturally weighted D array 6 cm map (the latter two, if they exist, cf. Table 2). Following these are a series of derived maps, i.e. spectral index, total energy, and magnetic field (§4.3) if they exist. Contour levels and/or greyscale ranges for all displayed maps are given in Tables A1 to A5. Note that all displayed intensity maps are uncorrected for the primary beam, but all derived maps (e.g. spectral index, etc.) and other derived quantities include the primary beam correction.

4.1. Extra-Planar Radio Continuum Emission

4.1.1. *Optical and Radio Dimensions of the Galaxies*

In Table 3 we present a comparison between the optical and radio dimensions of the galaxies. The radio dimensions are strongly dependent on the array and the weighting. This is also true of the semi-minor to semi-major axis ratio, b/a , because convolution with a large beam selectively increases b with respect to a . Thus, for the radio dimensions of Table 3, we have chosen the C array uniformly weighted data which has the highest spatial resolution and for which the minor axis emission is well resolved (for example, there are at least 2.7 and up to 9 beams across the radio minor axes with an average of 5.3 for

³DSS images were acquired via the SkyView website developed and maintained under the NASA ADP Grant NAS5-32068.

the galaxy sample). We then used a deconvolution algorithm to spatially deconvolve the known beam from the emission over the entire galaxy before listing the linear dimensions (Columns 4, 5). All measurements are to the 2σ level. With this correction, the ratio, radio b/a (Column 7), is 11% (on average) *lower* than it would be by taking the apparent radio minor to major axis ratio without the correction.

The median value of b/a for the optical measurements is 0.23 with a standard deviation of 0.04, while the median radio ellipticity is 0.38 ± 0.10 . The largest differences are for galaxies NGC 4746, NGC 4157, and NGC 3044 whose radio b/a range from 1.7 to 4 times the optical b/a. In only two cases (NGC 2613 and NGC 4517) is the radio b/a equivalent to or smaller than the optical value.

4.1.2. *Discrete Radio Extensions*

Every edge-on galaxy (Appendix A) shows radio spurs or discrete features extending in a direction away from the major axis (when each total intensity image is examined), with the possible exception of NGC 5297 and NGC 5433 whose discrete features are marginal. Also, in a few cases, namely IC 0564, NGC 3735 and NGC 4517, the apparent extensions are point-like and/or disconnected from the major axis emission and are therefore discounted as background sources. Thus 11 of 16 galaxies show discrete vertical radio extensions. In all of these galaxies, at least one or more radio features extend beyond the optical disk (see overlay of the first image or subsequent maps showing optical axes) indicating that they are extra-planar features.

There are also discrete features which project against the optical disk of the galaxy and which may or may not be out of the plane. Such features do not have the appearance of in-plane structures which usually trace spiral arms. For example, a single radio spur on the

north-west side of NGC 2683 (see radio contours over optical image) is projected against the background optical disk. If this feature were in the plane, it would delineate a radial radio feature extending over 3 kpc, isolated from the bulk of the radio emission interior to it and with no counterpart on the other side. Since we know of no precedent for such radio features in the disk and, by analogy with the known extra-planar spurs, we also interpret smaller discrete features such as the one described as extending out of the plane.

The discrete features appear to originate in the galaxy disk from various positions along the major axis. Consequently, searching for high latitude radio continuum emission by only taking slices along the minor axis would be insufficient to detect them. This also suggests that they originate with disk-related, rather than nucleus-related, phenomena. Possible exceptions in our sample are NGC 3044, which shows a large spur over the nuclear region and the well-defined and well-known nuclear radio lobes of NGC 4388 (Hummel et al. 1983; Wehrle 1987; Stone et al. 1988; Hummel & Saikia 1991) which are visible as a bulge in the contours on either side of the nucleus in the 20cm C array images of Appendix A. Large extensions are also visible on the 20 cm D array image, some of which could also be related to the nuclear outflow. However, the significance of the lower contour levels in this particular map is uncertain because of cleaning difficulties in the environment of other radio bright Virgo Cluster galaxies.

Even for these two galaxies in which nuclear features may be present, there are also other discrete features which appear to originate in the disk. See, for example, smaller extensions on the western major axis of NGC 3044 (C array naturally weighted data). For NGC 4388, there is a striking extension to the north, originating in the eastern major axis as seen in the 6 cm D array data. Whether this feature extends as far as implied in this image is uncertain (see above) but the reality of an extension at this position is not in question because a disturbance is also seen in the independent 20 cm C Array image and

an extension is also seen at this position in an HI image kindly supplied by J. van Gorkom.

4.1.3. *Radio Continuum Halos – Modeling a Thin Disk*

The D array naturally weighted images (Appendix A) show considerable emission beyond the projection of the optical minor axis. However, since beam smearing should be most pronounced for this lowest resolution data set, some or all of this emission could simply be due to beam smearing. To investigate this, we have generated a thin disk model galaxy for all cases for which D array observations exist (10 galaxies in total, Table 2, since the D array map for NGC 1421 was poor) and smoothed the inclined thin disk with the known beam to compare with observations. A thin disk (and its corresponding minimum inclination, cf. Column 8, Table 1) is adopted so as to be conservative and assume that as much emission as possible is due to the projection of in-plane emission against the sky. Thus, if anything, we will underestimate the extraplanar radio emission. We adopted a gaussian intensity distribution along the major axis and matched the model major axis extent to the observed radio continuum major axis at the 2σ level. This procedure is similar to that followed by Dahlem et al. (1997) except that we have allowed for a non-uniform major axis intensity distribution and we also model the entire thin-disk distribution, rather than taking only a single slice along the minor axis. The results are shown in Fig. 1 in which the smoothed model (heavy dashed contour) is plotted over the observed distribution (thin solid contours). Fig. 1 gives a visual impression of total radio power in the halo compared to the disk, for a disk conservatively chosen to contain as much power as possible.

For almost all galaxies, there is some evidence for extended emission (beyond the smoothed thin disk model) in a direction perpendicular to the major axis. The most obvious examples are NGC 2683, NGC 3432, NGC 3556, NGC 4388, and NGC 5775. Galaxies which show less obvious extensions or halos are NGC 2613 (the large south-western feature

could be a background source), NGC 3044, NGC 3221, and NGC 5297. The remaining galaxy for which D array naturally weighted data exist, NGC 4517, shows little evidence for extensions with the possible exception of two weak features (left top) on either side of a strong background point source.

Even in these low resolution maps, the extended emission often has structure. For example, radio spurs are seen in NGC 3221, and NGC 5775 and larger discrete extensions are seen in NGC 2683. The existence of structure far from the plane has been pointed out before for NGC 3432 by English and Irwin (1997) and from deeper observations of NGC 5775 (see Irwin 1995). Generally, as resolution improves, more discrete structures appear.

4.1.4. Prevalence of High Latitude Radio Continuum Emission in the Galaxies

Since the detection of high latitude radio continuum emission is dependent on sensitivity to various spatial scales, we have combined the above results in order to rank the observed galaxies according to the visibility of their extended radio emission as follows. Galaxies with b/a (radio) $> f$ b/a (optical) are given a weight of 2 for $f \geq 2$, 1 for $1 < f < 2$, and 0 for $f \leq 1$ (see §4.1.1). Galaxies which show discrete extensions beyond the optical disk are given a weight of 2, marginal cases are given a weight of 1, and galaxies where there is no evidence for discrete sources or the features are suspected of being background sources are given a weight of 0 (outlined in §4.1.2). Finally, galaxies with obvious radio halos or extensions beyond a modeled thin disk (D array natural weight data) are given a weight of 2, less obvious cases a weight of 1, and no evidence, a weight of 0 (see §4.1.3). Those galaxies for which D array data exist are ranked out of a total of 6 and those galaxies for which D array data do not exist are ranked out of a total of 4. Using all 3 criteria allows us to take into account evidence for high latitude radio continuum emission over a variety

of spatial scales from high resolution (C array uniform weight b/a ratio), to intermediate resolutions (discrete features beyond the optical disk as illustrated in Appendix A) to low resolution (D array thin disk modeling). (Note that we do not attempt to make corrections for differences in UV coverage.) Higher values, therefore, indicate that high latitude radio continuum emission is prevalent over many spatial scales and/or that the emission is stronger at any given spatial scale.

The results are shown in Column 3 of Table 6. Only one galaxy, NGC 4517, shows no evidence for extended radio continuum emission on any scale. This is also the galaxy in our sample which has the largest angular size (10.5 arcmin, cf Table 1); however, we should have detected high latitude radio continuum emission in this galaxy, if it exists, on spatial scales up to 15 arcmin (the largest angular size detectable at D array 20 cm). All other 15 galaxies show some evidence for extended high latitude radio continuum emission (a 94% detection rate), either a high radio b/a ratio, discrete extensions, smooth broadscale structure, or some combination of these. For 7 of these galaxies, extra-planar radio emission has been observed previously. These are: NGC 3044 (Hummel & van der Hulst 1989; Colbert et al. 1996), NGC 3221 (Hummel & van der Hulst 1989), NGC 3432 (English & Irwin 1997; same data), NGC 3556 (Bloemen et al. 1993), NGC 4157 (Hummel & van der Hulst 1989), NGC 4388 (nuclear outflow only; Hummel et al. 1983; Wehrle 1987; Stone et al. 1988; Hummel & Saikia 1991), NGC 5775 (Hummel et al. 1991; Irwin 1995). Thus, we have detected extra-planar radio continuum emission in 8 more edge-on galaxies. For two of these 8 galaxies (NGC 1421 and NGC 2683), some high latitude features can be similarly seen in the maps of Condon 1987.

4.2. Infra-Red and Radio Continuum Parameters

4.2.1. Fluxes, Luminosities, and Star Formation Indicators

In Table 4, we present total flux densities, luminosities, and other star formation indicators.

The flux density (Columns 2, 3) is measured from the lowest resolution D array naturally weighted maps, except for galaxies for which no D array data were available (cf. Table 2) and 3 galaxies for which the C array fluxes were considered to be more reliable. In the latter category, the galaxies are NGC 1421 (D array data were poor, possibly due to the low elevation of the source), NGC 3556 (the C array flux had a significantly smaller error bar but D and C array flux measurements agree to within errors) and NGC 2613 (the C array flux was higher than the D array flux and closer to previous literature values). All of our C array fluxes agree with a previously measured value (cf. Hummel 1980; Hummel et al. 1985; Condon et al. 1990) to within error bars or to within 10% when errors are not listed.

Using standard formulae (see Sanders & Mirabel 1996, their Table 1) we calculate a far infra-red luminosity L_{FIR} which represents emission in the $40\mu \leq \lambda \leq 120\mu$ range (uncorrected for longer wavelengths) and which is usually plotted in the FIR - radio continuum correlation. We also calculate the infrared luminosity L_{IR} which represents emission over $8\mu \leq \lambda \leq 1000\mu$ and is an indicator of luminous starbursts. The infrared flux densities used in these derivations were taken from the IR bright ($S_{60\mu} > 5.24$ Jy) sample catalogued in Soifer et al. (1989) if available (12 sources) which includes flux within ± 4 arcmin of each source position. The values for fainter sources, NGC 2613, NGC 4517, NGC 4746, and NGC 5297, were taken from the nearest positions in the Infrared Astronomical Satellite (IRAS) Point Source Catalog (PSC)(1988). (The association between the IRAS source and NGC 2613 is uncertain.) The latter values include flux only within the IRAS beam (1 arcmin) which is smaller than the optical extent of the galaxies.

However, most of the IR luminosity in galaxies is usually concentrated towards the central regions and we also find (see Fig. 2) that these galaxies fall on the FIR - radio continuum correlation, showing no significant discrepancies compared to galaxies which used the Soifer et al. IR fluxes. This suggests that the luminosities for these galaxies agree with those of Soifer et al. to within $\sim 20\%$.

For star formation rates (SFRs, Column 9), we follow Heckman et al. (1990) and compute this value for stars between 0.1 and $100 \mathcal{M}_\odot$ i.e. $\text{SFR}_{0.1 \rightarrow 100 \mathcal{M}_\odot} = 26 L_{\text{IR},11} (M_\odot \text{ yr}^{-1})$, where $L_{\text{IR},11}$ is the infrared luminosity in units of $10^{11} L_\odot$ (see also Hunter et al. 1986). This relation assumes that the bolometric luminosity, L_{bol} , is about equal to L_{IR} , an assumption which will underestimate the SFR because it is clear (cf. Columns 5 and 6) that there is at least a significant blue luminosity for these galaxies. We do not attempt to include L_B in our estimate of L_{bol} because of the unknown and variable internal extinction in these edge-on systems and also to be consistent with previous authors. The resulting SFRs can be compared to the value for the canonical starburst galaxy M 82 of $9 M_\odot \text{ yr}^{-1}$ (Heckman et al. 1990). By this measure, 6 of the galaxies in our sample could be considered starburst galaxies.

Column (10) lists the distance independent quantity, \dot{E}_A , which represents the rate of energy input into the ISM by supernovae per unit star forming area. This quantity is computed from $\dot{E}_A = \nu_{\text{SN}} E_{\text{SN}} / \pi r_{\text{SF}}^2 \text{ ergs s}^{-1} \text{ cm}^{-2}$, where $E_{\text{SN}} = 10^{51} \text{ ergs}$ is the energy input per supernova and $\nu_{\text{SN}} = 0.2 L_{\text{IR},11} \text{ SN yr}^{-1}$ is the supernova rate (Heckman et al. 1990). The computed supernova rates agree with those of Condon (1992) (who used L_{FIR} rather than L_{IR}) to within 5%.

For the star forming radius, r_{SF} , we use the highest resolution 20 cm C-array semi-major axis corrected for beam smoothing (Table 3). The star forming radius is probably the largest source of error on \dot{E}_A since its measurement depends on the rms noise

in the map as well as CR diffusion distances at the outer disk edge. The errors are in opposite directions, the former resulting in an underestimate of r_{SF} and the latter resulting in an overestimate of r_{SF} . To investigate the magnitude of these errors, we obtained a very deep H α image [peak signal-to-noise (S/N) ratio = 1200/1] of NGC 5775, kindly supplied by R.-J. Dettmar. For this galaxy, we find $r_{SF}(\text{H}\alpha) = 13.3$ kpc which differs from our radio radius of 12.6 kpc (Table 3) by only 5.3%. This translates into an 11% change in \dot{E}_A . Even though this is small, in the absence of information on the other galaxies, we have assumed that generous errors of up to 25% in r_{SF} could be present, resulting in error bars on \dot{E}_A of up to 50%.

The meaning of \dot{E}_A is the same as \dot{E}_A^{tot} of Dahlem, Lisenfeld, & Golla (1995), except that they have used the radio continuum power, rather than the IR luminosity to compute ν_{SN} (for the two galaxies which are common between the samples, NGC 3044 and NGC 5775, their ν_{SN} is $2.7 \times$ higher than ours). Their measurements of r_{SF} , which are also noise-dependent, are taken from either H α or IRAS CPC images.

4.2.2. FIR-Radio Continuum Correlation

Figure 2 plots the distance independent FIR-radio continuum correlation for the galaxies in our sample. The logarithmic measure of this correlation (Helou et al. 1985) is $q = \log [(L_{FIR}/3.75 \times 10^{12} \text{ Hz})/P_{20cm}]$, where L_{FIR} (W), P_{20cm} (W Hz^{-1}) are taken from Table 4. Excluding the Seyfert 2 galaxies, NGC 3735 and NGC 4388, we find a mean value for our sample of $q = 2.2$ and a dispersion of $\sigma_q = 0.1$. The latter value is comparable to the error in measurement. (Note that there would be no significant difference to q if the Seyfert, NGC 3735, were included since this galaxy also falls on FIR-radio continuum relation.) Our estimate of q is consistent with the value of 2.10 ($\sigma_q = 0.16$) for FIR luminous galaxies (Helou et al. 1985) and 2.3 ($\sigma_q = 0.2$) for normal galaxies (Condon 1992 and references

therein). The discrepant value for NGC 3432 is discussed in English & Irwin (1997).

The markers in Figure 2 indicate the supernova energy input rate per unit star forming area, from Table 4. There is a weak tendency for IR-luminous galaxies to also have a higher supernova energy input rate per unit area, but there are clear exceptions. Note the difference on the plot between NGC 4746 and NGC 3221, for example, or between NGC 2683 and NGC 3735 (each pair with similar values of \dot{E}_A).

4.2.3. *IR Surface Brightness – Colour Correlation*

It has been argued that a FIR flux ratio with $S_{60\mu}/S_{100\mu} > 0.4$ indicates that a galaxy may be IR warm (Heckman et al. 1990). Figure 3 plots this infra-red colour against the supernova energy input rate per unit star forming area. Since \dot{E}_A is obtained directly from L_{IR} (§4.2.1), this plot has the same meaning as the plot of IR surface brightness versus IR warmth given by Lehnert & Heckman (1996b) for starburst galaxies, except that we normalize by the radio continuum disk area, rather than the $H\alpha$ disk. Figure 3 confirms Lehnert & Heckman’s correlation, and extends their plot to lower surface brightnesses and cooler colours, i.e. this correlation also appears to apply to normal, as well as starburst galaxies. Lehnert & Heckman suggest that the dominant heating source for dust is UV radiation from hot stars, as opposed to heating by the general diffuse radiation field or an active galactic nucleus (AGN). The fact that we find a similar correlation using the radio continuum disk size (where the radio continuum is presumably correlated with the hot stars) appears to be consistent with their conclusion.

An exception to this relation is NGC 3432 which has a discordant SN input rate for its dust temperature. This difference reflects its offset position on the radio continuum – FIR correlation (Fig. 2), i.e. its IR luminosity is low in comparison to its radio continuum

power. If \dot{E}_A had been determined from radio continuum power, rather than IR luminosity, then this galaxy would have conformed to the general trend shown in Fig. 3.

4.3. Spectral Index, Energy, and Magnetic Field Maps

For the 5 galaxies with both 20 cm C array and 6 cm D array observations (NGC 1421, NGC 3044, NGC 3556, NGC 4388, and NGC 5775), we could obtain spectral index, α , maps ($S_\nu \propto \nu^\alpha$), as well as maps of total energy and magnetic field strength using the minimum energy assumption. These are shown in Appendix A with contour and greyscale levels listed in Tables A4 and A5. Some derived parameters from these maps are listed in Table 5.

4.3.1. Spectral Index Maps

Spectral index maps (Appendix A, Table A4) were made from the natural weighting 6 cm D array and natural weighting 20 cm C array data after smoothing to equivalent beams and applying a 1.5σ noise cutoff. The minimum, mean, and maximum values from these maps are listed in Columns (2) to (4) of Table 5. Values in parentheses represent corresponding values as measured from the uniform weighting spectral index maps which were similarly formed but are not shown.

Clearly, the steep spectral indices indicate that the emission is dominated by non-thermal components (see also Niklas et al. 1997). The thermal contribution from these galaxies is unknown; however, if we use the guidelines outlined in Condon (1992), then the non-thermal spectral index, α_{NT} , will be 0.1 to 0.3 steeper than the observed spectral index, for α ranging from -0.6 to -1.03, respectively (Table 5). The uncertainty in α is also of order 0.1. Since the observed variations in α are of magnitude 1 to 2 (Table

A4), structure in the maps is dominated by variations in the non-thermal spectral index.

Large variations in α can also be seen in a direction away from the major axis, indicating that there are real differences in α_{NT} between the disk and halo. The differences are in the sense of steeper (whiter on the maps) α_{NT} away from the plane. Duric, Irwin & Bloemen (1998), in a sensitive radio continuum study of NGC 5775, have suggested that such a gradient is due to the superposition of a steep spectral index halo and a flatter spectral index disk. There is also some evidence for steeper spectral indices in positions near discrete vertical extensions. For example, a steep spectral index is seen in NGC 1421 just at the base of a vertical extension on the west side of the galaxy (at $3^{\text{h}} 40^{\text{m}} 7^{\text{s}}.5$, $-13^{\circ} 38' 30''$). NGC 3044 shows strong steepening of the spectral index on either side of the radio continuum peak where vertical extensions are visible (see $9^{\text{h}} 51^{\text{m}} 8^{\text{s}}$, $01^{\circ} 49' 15''$ and $9^{\text{h}} 51^{\text{m}} 5^{\text{s}}$, $01^{\circ} 48' 25''$). Similarly, NGC 3556 and NGC 5775 both show steepening of the spectral index away from the major axis, especially in regions where extensions occur. The exception appears to be the Seyfert/AGN galaxy, NGC 4388, which displays a flat spectral index in the region of the nuclear outflow. If flatter spectral indices occur in regions of active winds (see also Fig. 2c of Duric et al. 1998), then steeper spectral indices near large discrete vertical features may be typical of older features where the active winds have ceased.

4.3.2. *Energy and Magnetic Field Maps*

Using the minimum energy assumption, it is also possible to obtain maps of magnetic field strength, B_{min} , and CR energy density, $u_{\text{min}}^{\text{CR}}$, averaged over a line of sight. These are computed (see Pacholczyk 1970; also see Duric 1991), in cgs units, from:

$$B_{\text{min}} = [6 \pi (1 + k) c_{12} V^{-1} L]^{2/7}$$

$$u_{min}^{CR} = (1 + k) c_{12} V^{-1} B_{min}^{-3/2} L$$

where k is the heavy particle to electron ratio, V is the volume, L is the luminosity, and c_{12} is one of “Pacholczyk’s constants” which, for the convention $S_\nu \propto \nu^\alpha$, is determined from:

$$c_{12} = 1.06 \times 10^{12} \left(\frac{2\alpha + 2}{2\alpha + 1} \right) \frac{[\nu_1^{(1+2\alpha)/2} - \nu_2^{(1+2\alpha)/2}]}{(\nu_1^{1+\alpha} - \nu_2^{1+\alpha})}$$

Here ν_1, ν_2 are the lower and upper frequency cut-offs and α is the spectral index.

We adopt the parameters, $k = 40$, $\nu_1 = 10^7$ Hz (the conventional value), and $\nu_2 = 10^{11}$ Hz. Since the luminosity, volume, and spectral index all vary across the galaxy, we compute the above quantities pixel-by-pixel, taking $V = r^2 l$, where r is the length of a pixel side and l is the line of sight distance through the galaxy at that pixel. Each map therefore required 3 input maps: the natural weighting 20 cm flux density map from which the luminosity is computed, the matching resolution spectral index map, and a map of line of sight distances, l . The latter was generated by assuming a spheroidal model galaxy which is inclined by the upper limit inclination (Table 1) with semi-major axis, a , set to match the observed value, and an intrinsic axial ratio, c/a , adjusted so that the model minor/major axis ratio (Table 3) also matched the observations. The resulting u_{min}^{CR} and B_{min} maps are shown (major axis horizontal) in Appendix A. Mean, minimum and maximum values from the u_{min}^{CR} and B_{min} maps are presented in Table 5. Again, using the guidelines outlined in Condon (1992), we find that a thermal contribution should change u_{min}^{CR} and B_{min} by less than 10%

Choosing a thin disk model to compute line of sight distances, changing the inclination to the lowest possible value (cf. Table 1), adopting a lower upper-frequency cutoff, or a different galaxy centre also each result in errors of order 10%. Differences between the 2 weightings of the data (i.e. different beam sizes) can be 30%, and adopting a different heavy particle to electron energy ratio, k (which can range from 1 to 100 in the literature) can produce an uncertainty of order a factor of 2. Thus the final values should be correct

to within factors of 2 - 3. However, the maps should illustrate the spatial variation in these values to a higher degree of accuracy (i.e. to $\lesssim 50\%$), since the same values of k and upper frequency cutoff are used for each point.

There is some evidence that when the in-disk energy and magnetic field strengths are higher (whiter on the maps), there is a greater probability that the radio continuum emission will be more extended in regions on either side of this emission. For example, NGC 1421, NGC 3044, and NGC 5775 all show broader (in the z direction) radio continuum emission on either side of brighter in-disk regions. On the other hand, a distinct radio spur in NGC 1421 is above a region of weak energy in the disk and the aforementioned correlations are not particularly obvious in either NGC 3556 or NGC 4388. Thus, there appears to be only a weak correlation, if any, between site of high energy and magnetic field and the presence of high latitude radio continuum emission.

4.3.3. *Cosmic Ray Lifetimes and Propagation*

Table 5 also presents estimates of CR age, τ_{CR} , Alfvén velocity, v_A , (Pacholczyk 1970) and diffusion length, which gives the distance a cosmic ray particle could travel before decaying (from $\tau_{CR}v_A$). The latter two quantities vary with the ISM density which is unknown and will vary within and between these galaxies. We adopt a typical Galactic value of 0.18 cm^{-3} which provides an estimate only of these quantities. Nevertheless, it is clear that the diffusion lengths (Column 13), which range from 1.4 to 4.9 kpc, are systematically less than the maximum vertical extent of the observed extra-planar radio emission (corrected for beam smoothing), i.e. 8 kpc for NGC 1421, 8 kpc for NGC 3044, 10 kpc for NGC 3556, 11 kpc for NGC 4388 (if real, see §4.1.2), and 18 kpc for NGC 5775. For the diffusion length to match the observed distribution, the mean ISM density would have to be as low as 0.002 to 0.04 cm^{-3} which is unlikely to be the case over most of the

ISM in these galaxies. This suggests that a) the high latitude radio continuum features exist because CRs diffuse through low density “chimneys” (Norman & Ikeuchi 1989) or intercloud regions (see Duric et al. 1998), and/or b) an additional mechanism is required to move the CRs to high latitude, examples being CR “winds” (see Bloemen 1991 and references therein), Parker instabilities (Kamaya et al. 1996), or ram pressure stripping. A similar conclusion was reached for NGC 3432 by English & Irwin (1997).

5. Discussion

The 16 edge-on galaxies in this sample are all star forming galaxies which represent a variety of star formation rates, type, degree of interaction and nuclear activity. Yet all of them, except NGC 4517, show some evidence for extended radio continuum emission away from the plane apparently originating in the disk. This suggests that high latitude radio continuum emission is common in star forming disk galaxies, in contrast to the results of Hummel et al. (1991) (see §2). The difference is probably due to our choice of longer wavelength (20 cm rather than 6 cm), and target galaxies of larger angular size (up to $10.5'$ rather than $< 4'$; see comments on resolution below).

In Table 6 we list the radio ranking, from §4.1.4, where galaxies are ranked out of 6 if there were additional D array data for them and out of 4 if not. We take the error bar on the ranking to be the width of the bin. In addition, we list the star formation rate ($\text{SFR}_{0.1 \rightarrow 100 M_{\odot}}$) and the supernova energy input rate per unit star forming area (\dot{E}_A) both from Table 4 and listed in order of decreasing \dot{E}_A . We also list the galaxy type (including Seyfert designation, if relevant), and information as to whether the galaxy appears to be isolated, have companions, is in a group or cluster, or is interacting. The latter information

is taken from the NASA/IPAC Extragalactic Database (NED) ⁴ and the references, notes, and catalogues therein. Before searching for correlations between the radio rank and other properties of the sample, however, we must first consider how S/N ratio and resolution might affect the results.

We computed a S/N ratio for each galaxy in two different ways. First, for each array configuration from which the radio rank was determined, we took the peak galaxy intensity divided by the noise in the map and then averaged these ratios to acquire a S/N for each object. Second, we found the ratio of total flux (Table 4) to noise (Table 2). The first method assumes that high latitude radio emission may scale with a local SFR (which is measured by the radio continuum brightness) and the second method assumes that high latitude radio emission may scale with a global SFR (as measured by the radio continuum flux). By the first method, the galaxies with the lowest S/N are NGC 5297, NGC 4517, and NGC 4746. By the second method, the galaxies with the lowest S/N are NGC 4388, NGC 3221, and NGC 5297. If our results depend strongly on the S/N ratio (and if the radio emission scales as we have assumed) then these low sensitivity galaxies should have the lowest radio rankings. From Table 6, however, other than NGC 4517, these galaxies do show significant evidence for radio halos. Galaxies such as NGC5433, NGC 3735, and IC 0564, for example, have significantly higher S/N (by both measures) than these, yet lower radio rankings. Even NGC 4517, which shows no high latitude radio emission, has a higher S/N (by the first method) than NGC 5297 (which does have high latitude emission) and a significantly higher S/N (by the second method) than NGC 4388, NGC 3221, and NGC 5297 (each of which has high latitude emission). Thus, while S/N must matter at

⁴The NASA/IPAC Extragalactic Database (NED) is operated by the Jet Propulsion Laboratory, California Institute of Technology, under contract with the National Aeronautics and Space Administration.

some level, the radio rankings of Table 6 do appear to be reflecting real differences between radio halos in these galaxies.

As for resolution, all the galaxies are reasonably well-resolved along their minor axes. For the C array uniformly weighted data, for example, there are between 2.7 and 9 beams across the minor axis (§ 4.1.1). The galaxies which have the fewest beams per minor axis are IC 0564, NGC 3735, and NGC 5433 and these do indeed have the lowest radio rankings (other than NGC 4517). Thus the probability of detecting extended radio emission does appear to improve with spatial resolution. One might expect that lower resolution observations would be more likely to detect radio halos because halos are considered to be broad-scale and smooth. However, we found (§4.1.3) that more discrete features appear as the resolution improves and that discrete features can sometimes be seen on the largest scales. This suggests that radio “halos” consist, at least in part and possibly entirely of discrete features combined with low spatial resolution. Timescale arguments are consistent with this hypothesis. We have shown (§4.3.3) that general diffusion of CRs in the vertical direction over the entire star forming disk, such as would produce a smooth halo, cannot account for the high latitude radio continuum emission observed. Other than the 3 low-resolution galaxies listed above, all other galaxies in the sample have between 4 and 9 beams per minor axis. An examination of the discrete features which are well-resolved suggests that 4 beams per minor axis appear to provide sufficient resolution to detect such features, if they exist. In the following sections, therefore, when we search for correlations between the radio ranking of the galaxies and other properties, we will do so for all the galaxies first, and then excluding the 3 low-resolution galaxies: IC 0564, NGC 3735, and NGC 5433.

Finally, when searching specifically for correlations with star formation indicators (§ 5.1, § 5.2) the AGN in the sample could be excluded because of the possible non-starburst

nature of their high latitude emission. There are two Seyfert galaxies in the sample (NGC 4388 and NGC 3735), but only one of them (NGC 4388) shows evidence for a radio AGN and does not fall on the FIR-radio continuum correlation (see Fig. 2). NGC 3735 does fall on the FIR-radio relation, suggesting that its nuclear activity is a minor contributor to the global radio flux. In addition, while the star forming galaxy, NGC 3432, does not have an AGN, it is peculiar in that it does not fall on the FIR-radio relation. Thus, for correlations with star formation indicators, we will first consider all galaxies and then exclude both NGC 4388 and NGC 3432 from the discussion due to their non-conformity to the FIR-radio relation.

“Radio halos”, below, is meant to mean any extra-planar radio continuum emission, as measured by the radio ranking listed in Table 6.

5.1. Radio Halos as a Function of Global Star Formation Rate

A comparison of the SFR with the radio ranking (Table 6), shows no obvious correlation. For example, of the 5 starburst galaxies ($\text{SFR}_{0.1 \rightarrow 100 M_{\odot}}$ greater than the M 82 value of $9 M_{\odot} \text{ yr}^{-1}$, see also Fig. 2) only one (NGC 5775) has very strong extra-planar radio emission. Galaxies with very low star formation rates (NGC 2683 and NGC 3432), on the other hand, can have significant extra-planar radio emission. With 5 galaxies excluded as explained above (3 because of low resolution and 2 because of non-compliance to the FIR-radio continuum relation), the conclusion is the same. To put this more quantitatively, we computed the linear correlation coefficient between SFR and radio ranking, with the radio ranking weighted (as to whether the observations are ranked out of 4 or 6). The correlation coefficient for all 16 galaxies is -0.29 and, for the subset of 11 galaxies, it is 0.007, in either case, significantly less (in absolute value) than 1. Thus, there is no correlation between radio rank and global SFR.

5.2. Radio Halos as a Function of \dot{E}_A

From a sample of 9 edge-on galaxies, Dahlem et al. (1995) found some evidence to suggest that it is the energy input rate per unit star forming area, \dot{E}_A , rather than the global SFR, which determines whether or not radio halos will be present.

Again, a comparison of \dot{E}_A with the radio rank (Table 6) shows no clear correlation. Galaxies with strong radio halos, for example, occur over a wide range of \dot{E}_A (cf. NGC 5775, NGC 3556, and NGC 3432). For the complete set, the weighted correlation coefficient (as described above, but using \dot{E}_A rather than SFR) is 0.18. Taking into account errors of up to 50% on \dot{E}_A (see § 4.2.1) in various ways (e.g. random, systematic) cannot increase the coefficient by more than $\sim 20\%$.

Excluding the 5 galaxies listed above, the correlation coefficient increases to 0.42. (Again, this cannot increase significantly, when errors in \dot{E}_A are taken into account.) The probability that a correlation coefficient this high or higher could occur from a random sample of the same size is 20%. Thus, there could be a weak correlation between these two properties for the subset of galaxies, but it is far from convincing.

The one galaxy, however, with the lowest value of \dot{E}_A (i.e. NGC 4517) shows no evidence at all for extra-planar radio emission. Dahlem et al. have suggested that there exists a lower cutoff to \dot{E}_A below which “blowout” cannot occur, and therefore a radio halo will not form. Our data suggest that, if such a threshold exists, it would be at $\approx 0.04 \times 10^{-3} \text{ erg s}^{-1} \text{ cm}^{-2}$, i.e. the level observed for NGC 4517. Correcting for the different methods of computing ν_{SN} (see § 4.2.1), this value does agree with the lower threshold of $10^{-4} \text{ erg s}^{-1} \text{ cm}^{-2}$ given by Dahlem et al. (1995).

Thus, our results are consistent with the existence of a lower threshold to \dot{E}_A for the formation of a radio halo but, at best, allows for only a weak correlation between \dot{E}_A and

the strength of the radio halo as we have defined it amongst a subset of the galaxies.

5.3. Radio Halos as a Function of Galaxy Type

We find no relation between the presence of high latitude radio continuum and Hubble type, or the presence or absence of bars, although the latter may be rather difficult to classify, given the edge-on orientation of the galaxies. With the 3 low-resolution galaxies excluded, again there is no correlation. The two Seyfert galaxies, NGC 3735 and NGC 4388 also show very different levels of extended radio emission.

5.4. Radio Halos as a Function of Galaxy Environment

This issue is more difficult to assess since it is not always clear whether the presence of a companion implies an interaction. It is now recognized that even when an interaction is in progress, a starburst may or may not be occurring depending on the details and timing of the event (Mihos & Hernquist 1996). Table 6 indicates that most of the galaxies in the sample are not isolated. Only three galaxies, NGC 3044, NGC 3556, and NGC 1421 might arguably be considered isolated. Yet all three show strong evidence for high latitude radio continuum emission and two of these are known to have high latitude HI shells (NGC 3044: Lee & Irwin 1997; NGC 3556: King & Irwin 1997). Thus, it would appear that interactions are not necessary to produce radio halos.

It has been suggested, however, that interactions may enhance radio halos due to gravitational perturbations for cases in which the SFR is relatively low (e.g. NGC 4631, Dahlem et al. 1995; NGC 3432, English & Irwin 1997). In our sample, the galaxies with the lowest values of \dot{E}_A are NGC 3432, NGC 2613, NGC 5297, and NGC 4517. Of these, the first 3 are either interacting or in a group and also show evidence for radio halos,

NGC 3432 having the strongest. NGC 4517 does not have a radio halo but is paired with UGC 07685 and could also be in a small group. Thus, while the data do not rule out this possibility, they do not strongly support it either. Nothing more definitive can be said if the 3 low-resolution galaxies are excluded. It will likely take a larger sample with better understood interaction properties to adequately investigate this possibility.

Another way in which environment may play a role in forming extra-planar features is through ram pressure stripping. Virgo Cluster galaxies, such as NGC 4388 (see §4.1.2), may fall into this category (see Cayatte et al. 1990).

5.5. Radio Halos as a Relic of Past Activity

For the 5 galaxies for which we could compute radio properties (Table 5), mean CR lifetimes range from 3×10^7 yr to 1.3×10^8 yr. Using the lower magnetic field strengths which occur in the halo regions, this range increases to 6×10^7 yr to 2×10^8 yr. Thus, in general, the lifetime of halo CRs in these galaxies is $\approx 10^8$ yr.

The lifetime of any given OB association is of order a few $\times 10^7$ yr. Thus, if cosmic rays escape from the disk over specific star forming regions, the resulting discrete feature may remain visible even after the region below it has ceased to be actively star-forming. While star formation can take place globally over longer timescales, this effect could still mask or weaken a correlation between radio halos and SFR or between halos and \dot{E}_A , if either correlation existed initially. The effect should be strongest for starbursts. Theoretical models of starbursts in mergers suggest starburst durations of $\approx 5 \times 10^7$ yr (Mihos & Hernquist 1996). Recent Infrared Space Observatory observations of luminous IR galaxies are also suggesting relatively short starburst durations of $1 - 2 \times 10^7$ yr (Lutz et al. 1996). Thus if a radio halo has resulted from starburst activity, it could remain even after all

evidence for the starburst has disappeared. This could explain why we do not see a clear correlation between radio halos and \dot{E}_A (§5.2). A search for correlations between discrete flat spectral index features (e.g. a signature of active winds) and in-disk star forming regions, or between shorter-lived high latitude features (such as extra-planar $H\alpha$) and in-disk star forming regions may be more fruitful.

6. Conclusions

We have observed 16 edge-on galaxies in the radio continuum using the VLA at 20 cm in its C configuration and have supplemented this with 6 and/or 20 cm data in D configuration for a subset of the galaxies. The range of spatial scales probed is $11''$ to either $4'$ (C array 20 cm data) or $15'$ (D array 20 cm data) compared to the optical dimensions of the galaxies which range from $1.6'$ to $10.5'$. The sample was chosen by high inclination, by angular size, and by radio flux density and represents a wide range of star formation rates (only 6 galaxies are starbursts), Hubble type, and degree of isolation or interaction. The purpose of the survey was to search for high latitude ($\gtrsim 1$ kpc) radio continuum emission.

Of these 16 edge-on galaxies, we find that all but one galaxy (NGC 4517) show evidence for such emission. Of these, 8 are new detections. Thus, extra-planar radio emission appears to be common in star forming galaxies. The radio emission is seen on a variety of scales and in a variety of ways, including large radio axial ratios (b/a), the presence of discrete features extending away from the major axis, or broad scale emission extending beyond the projection of a modeled thin radio disk. Discrete features can be seen on a variety of spatial scales including the broadest scales, suggesting that radio halos may, in part and perhaps completely, be discrete features as seen with large beams. Indeed, high resolution appears to be necessary to detect high latitude features. Nuclear outflow is seen in the case of the Seyfert/AGN NGC 4388 and radio spurs seen in NGC 3044 could originate from

its nucleus. However, even in these galaxies there is evidence for some disk features and discrete features appear to originate in the disk in all other cases.

For 5 galaxies, we could form maps of spectral index, CR energy density and magnetic field strength. The emission is predominantly non-thermal and variations in the maps are significantly greater than variations expected from a thermal contribution. The spectral index shows steepening away from the plane in regions of discrete extensions but there is no strong correlation between high latitude radio features and the energy or magnetic field strength. Diffusion alone appears to be insufficient to transport CRs to high latitude for reasonable mean ISM densities. Thus, they could be transported through low density regions and/or assisted by other mechanisms such as winds.

All galaxies, with the exception of the Seyfert/AGN, NGC 4388, and the low SFR galaxy, NGC 3432 (see English & Irwin 1997) fall on the FIR - radio continuum correlation. In addition, we have extended the IR surface brightness – colour relation found for starburst galaxies by Lehnert & Heckman (1996b) to the lower SFR galaxies of this sample.

We have ranked the galaxies into broad categories, depending on the strength and extent of the extra-planar radio emission over all detectable scales, and have searched for correlations between radio rank and other properties, including global SFR, supernova energy input rate per unit area, \dot{E}_A , galaxy environment, and galaxy type. We find no clear correlation with the latter two properties. It is difficult to assess the correlation between radio rank and galactic environment, however, since the degree to which a galaxy may be interacting is not always clear. Thus a larger sample is likely needed. Nevertheless, since 3 apparently isolated galaxies do have strong radio halos, it would appear that interactions are not necessary to generate high latitude radio emission.

We find no clear correlations with either SFR or \dot{E}_A . If we exclude 5 galaxies because of low resolution or non-compliance with the FIR-radio continuum relation, then the data

allow for a weak correlation with \dot{E}_A (correlation coefficient of 0.4), but the result is not convincing. The one galaxy with no evidence for high latitude radio emission (NGC 4517) does, however, have a value of \dot{E}_A which agrees with the lower threshold given by Dahlem et al. 1995. The lack of a good correlation between radio halos and \dot{E}_A might be explained by the difference in timescales. With lifetimes of $\sim 10^8$ yr, radio halos may represent the integration of star formation activity over that timescale, whereas quantities such as SFR and \dot{E}_A represent (in comparison) snapshots of activity which might last for $\sim 10^7$ yr in specific star forming regions or $\lesssim 5 \times 10^7$ yr for starbursts. Thus, if a radio halo – starburst correlation originally exists, it may weaken with time. This suggests that it may be better to search for correlations between \dot{E}_A and extra-planar H α emission or to search for correlations between discrete flat-spectral index features (such as would indicate the presence of active winds) and in-disk star forming regions in order to search for a starburst origin for the high latitude features. If high latitude radio continuum emission does result from star forming activity, then the existence of a radio halo could provide a useful signature that a galaxy has indeed experienced a starburst in the past.

Acknowledgements: We gratefully acknowledge the assistance of Michael Earl in preparing the figures for publication. The Digitized Sky Surveys were produced at the Space Telescope Science Institute under U.S. Government grant NAG W-2166. The images of these surveys are based on photographic data obtained using the Oschin Schmidt Telescope on Palomar Mountain and the UK Schmidt Telescope. The plates were processed into the present compressed digital form with the permission of these institutions. We acknowledge the use of NASA’s *SkyView* facility (<http://skyview.gsfc.nasa.gov>) located at NASA Goddard Space Flight Center. This research has made use of the NASA/IPAC Extragalactic Database (NED) which is operated by the Jet Propulsion Laboratory, California Institute of Technology, under contract with the National Aeronautics and Space Administration. We are grateful to the Australia National Telescope Facility for the use of

their Karma software package.

Appendix A: Maps of 16 Edge-On Spiral Galaxies.

For individual galaxies, 1-2 pages are devoted to total intensity maps (synthesized beam is shown at bottom left of each) and derived spectral index and energy and magnetic field maps, if the latter are available.⁵ The maps are as follows:

1. Contours of uniformly weighted 20-cm C-array data overlayed on DSS. A logarithmic display of the B passband images is used so that the full optical extent of each galaxy is apparent. (This is the largest image and is at the top or lefthand side of the page.) Contour levels begin at 2σ and are listed in Table A1.
2. Contours (plus greyscale) of the naturally weighted 20-cm C-array data. The optical axes are shown and have arrow tips if they extend beyond the contour map. Optical data are taken from the RC3, or from NED if the latter values differ significantly from the RC3. Contour levels, beginning at 2σ , are listed in Table A1.
3. Contours (plus greyscale) of the naturally weighted 20-cm D-array data with optical axes shown. Contour levels, starting at 2σ , are listed in Table A2.
4. Contours (plus greyscale) of the naturally weighted 6-cm D-array data. Contour levels, starting at 2σ , are listed in Table A3.
5. Contours (plus greyscale) of spectral index data, where $S_\nu \propto \nu^\alpha$ (§ 4.3.1). White represents steep values of α while black represents flat α . Contour levels are listed in Table A4.

⁵The plots were made using Karma Visualization software developed by the CSIRO Australia Telescope National Facility.

6. Logarithmic greyscale of minimum energy in CRs (§ 4.3.2) with white representing high energy and black representing low energy. 20-cm C-array naturally weighted contours are overlaid. Contour levels and greyscale ranges are listed in Table A5.
7. Logarithmic greyscale of magnetic field maps (§ 4.3.2) with 20-cm C-array (naturally weighted) contours overlaid. Contour levels and greyscale ranges are listed in Table A5. White represents high magnetic fields and black represents low.

REFERENCES

- Beichman, C. A., Neugebauer, G., Habing, H. J., Clegg, P. E., & Chester, T. J., editors
1988, *Infrared Astronomical Satellite Point Source Catalog*, NASA (RP-1190)
- Bloemen, H. 1991, in *The Interpretation of Modern Synthesis Observations of Spiral Galaxies*, edited by Duric, N. & Crane, P. C., volume 18, page 27, A.S.P. Conf. Ser
- Bloemen, H., Duric, N., & Irwin, J. A. 1993, in *Proc 23rd International Cosmic Ray Conference*, edited by Leahy, D. A., Hicks, R. B., & Venkatesan, D., volume 2, page 279, World Scientific
- Bregman, J. N. 1980, *A&A*, 236, 577
- Cayatte, V., Balkowski, C., van Gorkom, J. H., & Kotanyi, C. 1990, *AJ*, 100, 604
- Chamaraux, P., Balkowski, C., & G'érard, E. 1980, *A&A*, 83, 38
- Colbert, E. J. M., Baum, S. A., Gallimore, J. F., O'Dea, C. P., & Christensen, J. A. 1996, *ApJ*, 467, 551
- Condon, J. J. 1987, *ApJS*, 65, 485
- Condon, J. J. 1992, *ARA&A*, 30, 575
- Condon, J. J., Helou, G., Sanders, D. B., & Soifer, B. T. 1990, *ApJS*, 73, 359
- Dahlem, M. 1997, *PASP*, 109, 1298
- Dahlem, M., Lisenfeld, U., & Golla, G. 1995, *ApJ*, 444, 119
- Dahlem, M., Petr, M. G., Lehnert, M., Heckman, T. M., & Ehle, M. 1997, *A&A*, 320, 731
- de Vaucouleurs, G. de Vaucouleurs, A. & Corwin, H. G. J. 1976, *Second Reference Catalogue of Bright Galaxies (RC2)*, University of Texas Press, New York

- de Vaucouleurs, G., de Vaucouleurs, A., Corwin, H. G., Buta, R. J., Paturel, G., & P., F. 1991, Third Reference Catalogue of Bright Galaxies (RC3), Springer-Verlag New York
- Dettmar, R.-J. 1992, *Fundamentals of Cosmic Physics*, 15, 143
- Dressel, L. L. & Condon, J. J. 1978, *ApJS*, 36, 53
- Duric, N. 1991, in *The Interpretation of Modern Synthesis Observations of Spiral Galaxies*, edited by Duric, N. & Crane, P. C., volume 18, page 17, A.S.P. Conf. Ser
- Duric, N., Irwin, J. A., & Bloemen, H. 1998, *A&A*, 331, 428
- English, J. & Irwin, J. A. 1997, *AJ*, 113, 2006
- Franco, J., Ferrini, F., Ferrara, A., & Barsella, B. 1991, *ApJ*, 366, 443
- Giuricin, G., Bertotti, G., Mardirossian, F., & Mezzetti, M. 1990, *MNRAS*, 247, 444
- Golla, G. & Hummel, E. 1994, *A&A*, 284, 777
- Heckman, T. M., Armus, L., & Miley, G. K. 1990, *ApJS*, 74, 833
- Helou, B., Soifer, B. T., & Rowan-Robinson, M. 1985, *ApJ*, 298, L7
- Howk, J. C. & Savage, B. D. 1997, *AJ*, 114, 2463
- Hummel, E. 1980, *A&AS*, 41, 151
- Hummel, E., Beck, R., & Dettmar, R.-J. 1991, *A&AS*, 87, 309
- Hummel, E., Pedlar, A., van der Hulst, J. M., & Davies, R. D. 1985, *A&AS*, 60, 293
- Hummel, E. & Saikia, D. J. 1991, *ã*, 249, 43
- Hummel, E. & van der Hulst, J. M. 1989, *A&AS*, 81, 51

- Hummel, E., van Gorkom, J., & Kotanyi, C. 1983, *ApJ*, 267, L5
- Hunter, D. A., Gillet, F. C., Gallagher, J. S., Rice, W. L., & Low, F. J. 1986, *ApJ*, 303, 171
- Irwin, J. & Sofue, Y. 1996, *ApJ*, 464, 738
- Irwin, J. A. 1991, in *The Interpretation of Modern Synthesis Observations of Spiral Galaxies*, edited by Duric, N. & Crane, P. C., volume 18, page 59, San Francisco: A.S.P.
- Irwin, J. A. 1994, *ApJ*, 429, 618
- Irwin, J. A. 1995, *PASP*, 107, 715
- Kamaya, H., Mineshige, S., Shibata, K., & Matsumoto, R. 1996, *ApJ*, 458, L25
- King, D. L. & Irwin, J. A. 1997, *New Astronomy*, 2, 251
- Lang, K. R. 1974, *Astrophysical Formulae*, page 558, New York: Springer-Verlag
- Lee, S.-W. & Irwin, J. A. 1997, *ApJ*, 490, 247
- Lehnert, M. D. & Heckman, T. M. 1996a, *ApJ*, 462, 651
- Lehnert, M. D. & Heckman, T. M. 1996b, *ApJ*, 472, 546
- Lutz, D., Genzel, R., Sternberg, A., Netzer, H., Kunze, D., Rigopoulou, D., Sturm, E., Egami, E., Feuchtgruber, H., Moorwood, A. F. M., & de Graauw, T. 1996, *A&A*, 315, L137
- Mihos, J. C. & Hernquist, L. 1996, *ApJ*, 464, 641
- Niklas, S., Klein, U., & Wielebinski, R. 1997, *A&A*, 322, 19
- Norman, C. A. & Ikeuchi, S. 1989, *ApJ*, 345, 372

- Oldenwald, S. F. 1986, *ApJ*, 310, 86
- Pacholczyk, A. G. 1970, *Radio Astrophysics: Non-thermal Processes in Galactic and Extragalactic Sources*, San Francisco: W. H. Freeman & Co.
- Phillips, M. M. & Malin, D. F. 1982, *MNRAS* 199, 905
- Sanders, D. B. & Mirabel, I. F. 1996, *ARA&A*, 34, 749
- Schneider, S. E., Helou, G., Salpeter, E. E., & Terzian, Y. 1986, *AJ*, 92, 742
- Shapiro, P. R. & Field, G. B. 1976, *ApJ*, 205, 762
- Sharp, N. A. 1990, *P.A.S.P.*, 102, 109
- Soifer, B. T., Boehmer, L., Neugebauer, G., & Sanders, D. B. 1989, *AJ*, 98, 766
- Sorathia, B. 1994, *A Radio Continuum Survey of Edge-on Spiral Galaxies*, Master's thesis, Queen's University
- Stone, J. L., J., Wilson, A. S., & Ward, M. J. 1988, *ApJ*, 330, 105
- Surace, J. A., Mazzarella, J., Soifer, B. T., & Wehrle, A. E. 1993, *AJ*, 105, 864
- Tully, R. B. 1988, *Nearby Galaxies Catalog*, Cambridge Univ. Press
- Turner, K. C., Helou, G., & Terzian, Y. 1988, *PASP*, 452, 457
- Vogler, A. & Pietsch, W. 1996, *A&A*, 311, 35
- Völk, H. J. 1991, in *The Interstellar Disk-Halo Connection in Galaxies*, edited by Bloemen, H., volume 144, page 345, I.A.U. Symp.
- Wehrle, A. E. 1987, *The Radio Structure of Active Nuclei in Edge-on Spiral and Seyfert Galaxies*, PhD thesis, California Univ., Los Angeles

Zaritsky, D., Smith, R., Frenk, C., & White, S. D. M. 1997, ApJ, 478, 39

Fig. 1.— Model thin disks are super-imposed as a thick dashed line on 20 cm D Array naturally weighted data (§ 4.1.3). For each image, the major axis has been rotated to align with the x axis and the first contour is at 2σ . See Appendix A for other, non-rotated displays of these data.

Fig. 2.— Radio Continuum – Far Infrared Correlation. The markers indicate supernova energy input rate per unit star forming area (cf. Table 4).

Fig. 3.— An estimate of the supernova energy input rate per unit star forming area is plotted against the dust temperature (FIR colour). See § 4.2.3.

TABLE 3. Comparison of Radio and Optical Galaxy Dimensions.

Name	Optical		Radio		b/a	
	a	b	a	b	Optical	Radio
	kpc	kpc	kpc	kpc		
(1)	(2)	(3)	(4)	(5)	(6)	(7)
NGC 1421	13.3	3.4	11.1	4.5	0.26	0.40
NGC 2613	27.1	6.8	21.2	4.1	0.25	0.19
NGC 2683	11.3	2.7	5.2	1.7	0.24	0.33
IC 0564	21.0	4.9	19.3	7.3	0.24	0.38
NGC 3044	15.5	2.2	8.1	4.6	0.14	0.56
NGC 3221	27.4	6.0	15.5	5.3	0.22	0.34
NGC 3432	11.6	2.6	7.1	2.4	0.22	0.33
NGC 3556	14.6	3.7	10.9	4.1	0.25	0.37
NGC 3735	22.6	4.3	16.9	4.9	0.19	0.29
NGC 4157	12.8	2.4	7.0	3.2	0.19	0.45
NGC 4388	16.3	3.8	5.8	2.2	0.23	0.38
NGC 4517	29.7	4.3	18.4	2.3	0.14	0.13
NGC 4746	15.4	4.5	6.9	3.4	0.29	0.50
NGC 5297	28.1	6.5	12.7	4.0	0.23	0.32
NGC 5433	14.1	3.5	10.1	4.4	0.25	0.44
NGC 5775	15.4	3.7	12.6	4.8	0.24	0.38

Notes to Table 3.

The optical semi-axes (2) and (3) are derived using the angular diameters in Table 1, converted to kiloparsecs. Radio semi-axes (4), (5), have been measured to the 2σ level from the C array uniformly weighted data and corrected for beam smearing before conversion to kpc (see §4.1.1). The semi-minor/semi-major axis ratios (6), (7) are computed from Column (2)/Column (3) and Column (4)/Column (5), respectively.

TABLE A3. Contour Levels for 6 cm D-array Maps

Galaxy	Levels (mJy beam^{-1})
NGC 1421	$0.116 \times (1, 2, 5, 7, 10, 15, 20, 30, 40, 50)$
NGC 3044	$0.0916 \times (1, 2, 3, 5, 7, 10, 15, 20, 30, 40, 50, 60, 70, 80, 90, 100)$
NGC 3556	$0.0927 \times (1, 2, 3, 5, 7, 10, 15, 20, 30, 40, 50, 60, 70, 80, 90, 100, 110, 120)$
NGC 4388	$0.105 \times (1, 2, 5, 10, 15, 30, 60, 90, 120, 150, 180, 210, 240, 270)$
NGC 5775	$0.139 \times (1, 2, 5, 10, 15, 25, 35, 45, 60, 75)$

TABLE 4. Fluxes, Luminosities and Star Formation Rate Indicators.

Name	S_{6cm} mJy	S_{20cm} mJy	$\log P_{20cm}$ $\log \text{ Watts Hz}^{-1}$	$\log (L_B/L_\odot)$	$\log (L_{IR}/L_\odot)$	$\log (L_{FIR}/L_\odot)$	S_{60}/S_{100}	S_{100}/S_{160}
(1)	(2)	(3)	(4)	(5)	(6)	(7)	(8)	(9)
NGC 1421	37 ± 7	89 ± 2 (C)	21.86	10.57	10.44	10.16	0.46	
NGC 2613 *		69 ± 4 (C)	21.74	11.01	10.29	10.00	0.33	
NGC 2683		84 ± 4 (D)	20.85	10.16	9.47	9.18	0.30	
IC 0564 ^a		37 ± 2 (C)	22.50	10.79	11.00	10.56	0.38	
NGC 3044	42 ± 7	106 ± 3 (D)	21.78	10.36	10.22	9.95	0.50	
NGC 3221		109 ± 2 (D)	22.66	10.62	11.00	10.72	0.38	
NGC 3432		120 ± 3 (D)	21.30	9.89	9.53	9.32	0.52	
NGC 3556	89 ± 7	279 ± 5 (C)	21.65	10.35	10.21	9.94	0.42	
NGC 3735		80 ± 4 (C)	22.12	10.70	10.62	10.32	0.38	
NGC 4157		202 ± 5 (C)	21.61	9.69	10.09	9.80	0.35	
NGC 4388	73 ± 7	200 ± 10 (D)	21.98	10.43	10.22	9.83	0.58	
NGC 4517 *		38 ± 4 (D)	21.24	10.74	9.83	9.57	0.27	
NGC 4746 *		46 ± 4 (C)	21.63	10.13	10.15	9.87	0.39	
NGC 5297 *		23 ± 5 (D)	21.52	10.67	10.12	9.80	0.27	
NGC 5433		59 ± 4 (C)	22.42	10.72	10.87	10.60	0.56	
NGC 5775	76 ± 11	275 ± 5 (D)	22.32	10.47	10.72	10.44	0.46	

Notes to Table 4.

Flux densities (2), (3) are measured from D array data (D) or C array data (C), see § 4.2. Error bars are the larger of a) $\sigma_{\text{beam}}/\sqrt{N}$ and N is the number of beams occupied by the galaxy, or b) the measured flux in an equivalent region of the background or c) the rms of different measurement regions. The radio power (4) is computed from $P_{20cm} = 4 \pi D^2 S_{20cm}$, with D from Column (3), D is derived from the total face-on apparent B magnitude (B_T^0) given in the RC3, using 5.41 for the absolute blue magnitude (M_B^0). Columns (6) and (7) list the IR and FIR luminosities, following Sanders & Mirabel (1996). Flux densities from Soifer et. al.(1989) were taken from the IRAS Point Source Catalog (1988) and are marked with a * in column (1). Ratios in column (8) are the star formation rate (9) and supernova input energy rate per unit star forming area (10) are described in § 4.2. *a)* IR Values from Soifer et. al. (1993) who resolved IC 0564 from its nearby companion, IC 0563.

TABLE A4. Contour Levels for Spectral Index Maps

Galaxy	Levels
NGC 1421	-1.4, -1.3, -1.2, -1.0, -0.9, -0.8, -0.7, -0.6, -0.5, -0.4
NGC 3044	-1.0, -0.9, -0.85, -0.8, -0.75, -0.7, -0.65, -0.6, -0.5, -0.4, -0.3, -0.1
NGC 3556	-1.9, -1.6, -1.5, -1.3, -1.2, -1.1, -1.0, -0.9, -0.85, -0.8, -0.7, -0.6, 0.0
NGC 4388	-1.5, -1.4, -1.3, -1.2, -1.1, -1.0, -0.9, -0.85, -0.8, -0.75, -0.7, -0.65, -0.6, -0.5, -0.30, -0.1, 0.0
NGC 5775	-1.7, -1.5, -1.3, -1.1, -1.0, -0.9, -0.8, -0.7, -0.6, -0.65, -0.5

TABLE 5. Radio Properties

Name	α			u_{\min}^{CR} $10^{-12} \text{ erg cm}^{-3}$			B_{\min} μGauss			τ_{CR} 10^6 yr
(1)	mean (2)	min (3)	max (4)	mean (5)	min (6)	max (7)	mean (8)	min (9)	max (10)	(11)
NGC 1421	-0.80 (-0.66)	-1.48 (-1.28)	-0.11 (0.21)	6.53	3.72	49.3	6.8	5.2	19.0	70
NGC 3044	-0.60 (-0.81)	-1.04 (-1.38)	0.22 (-0.13)	4.77	1.66	10.7	5.8	3.5	8.9	46
NGC 3556	-1.03 (-0.95)	-1.58 (-1.41)	-0.56 (-0.47)	6.76	4.00	15.5	7.0	5.4	10.7	132
NGC 4388	-0.78 (-0.76)	-1.52 (-1.15)	0.00 (-0.29)	18.4	9.24	33.1	11.6	8.3	15.6	30
NGC 5775	-0.93 (-0.97)	-1.81 (-1.92)	-0.18 (-0.14)	7.99	4.13	19.4	7.6	5.5	11.9	89

Notes to Table 5.

Columns (2) to (4) give the mean, minimum, and maximum spectral index measured from the natural weighting spectral index (A). Values in parentheses are measured from the uniform weighting maps (not shown). Columns (5) to (7) give the cosmic ray energy density and columns (8) to (10) give the magnetic field strength (mean, minimum and maximum from the natural weighting maps shown) assuming minimum energy. The CR lifetime, $\tau_{CR} \propto B_{\min}^{-3/2}$ (Column 11), and Alfvén velocity, $v_A = B_{\min}/\sqrt{4\pi\rho}$ (Column 12) are computed from the mean B_{\min} (Column 8). v_A is an order of magnitude estimate assuming a constant mean ISM density of 0.18 cm^{-3} for each source. The diffusion length (Column 13) is computed from $\tau_{CR} v_A$. (See Pacholczyk 1970, Duric 1991, and § 4.3.2 for more details.)

TABLE A5. Contour Levels and Greyscale Ranges for Energy and Magnetic Field Maps

Galaxy	u_{\min}^{CR} Range (erg cm ⁻³)	B_{\min} Range (Gauss)	20-cm C-array Contour Levels (mJy beam ⁻¹)
NGC 1421	3.72E-12 4.93E-11	5.23E-06 1.90E-05	0.187 × (1, 2, 5, 15, 20, 50)
NGC 3044	1.66E-12 1.07E-11	3.49E-06 8.85E-06	0.146 × (1, 2, 10, 15, 100)
NGC 3556	3.99E-12 1.55E-11	5.41E-06 1.07E-05	0.086 × (1, 2, 15, 30, 100)
NGC 4388	9.24E-12 3.31E-11	8.24E-06 1.56E-05	0.46 × (1, 2, 10, 25, 50, 100)
NGC 5775	4.13E-12 1.94E-11	5.51E-06 1.19E-05	0.184 × (2, 3, 10, 40, 80, 100)

TABLE 6. Degree of Extended Radio Emission

Name	$\text{SFR}_{0.1 \rightarrow 100 M_\odot}$ $M_\odot \text{ yr}^{-1}$	\dot{E}_A $10^{-3} \text{ erg s}^{-1} \text{ cm}^{-2}$	Radio Rank	Type	Environment
(1)	(2)	(3)	(4)	(5)	(6)
NGC 5433	19.3	1.56	2/4	Sdm:	possible 2 companions
NGC 4388	4.40	1.08	5/6	SA(s)b: sp Sy2	in Virgo Cluster
NGC 3221	26.0	0.88	4/6	SB(s)cd sp	3 companions
NGC 5775	13.7	0.70	5/6	SBc?	interacting ^c
NGC 4746	3.65	0.62	3/4	Sb: sp	in Virgo Cluster ^g
IC 0564	25.8	0.56	1/4	SA(s)cd? pec	pair ^h
NGC 3044	4.27	0.54	5/6	SB(s)c? sp	isolated
NGC 4157	3.18	0.52	4/4	SAB(s)b? sp	in UMa I(s) group
NGC 1421	7.21	0.48	3/4	SAB(rs)bc:	isolated ^f
NGC 3556	4.26	0.30	5/6	SB(s)cd	isolated ^b
NGC 3735	10.8	0.30	1/4	SAc: sp Sy2	2 companions ⁱ
NGC 2683	0.766	0.24	5/6	SA(rs)b	companion
NGC 5297	3.46	0.18	3/6	SAB(s)c: sp	interacting ^d
NGC 3432	0.886	0.14	5/6	SB(s)m	interacting ^a
NGC 2613	5.13	0.10	3/6	SA(s)b	in group
NGC 4517	1.76	0.04	0/6	SA(s)cd: sp	pair ^e

Notes to Table 6.

Columns (2) and (3) give the star formation rate and supernova energy input rate per unit area, respectively, as in Table 4, and are ordered according to \dot{E}_A . Column (4) gives the radio ranking which reflects the degree to which extra-planar radio emission is seen (see § 4.1.4). Galaxies with D array data are ranked out of 6 and galaxies without D array data are ranked out of 4 with higher numbers indicating stronger evidence for high latitude radio continuum emission. The galaxy's morphological type, including Seyfert designation where applicable, (Column 5) and comments as to whether the galaxy is isolated, has companions, is in a group or cluster, or interacting (Column 6) are taken from information in the NASA Extragalactic Database (NED). *a)* Arp 206 (with UGC 5983) *b)* Could be on the outskirts of the UMaI(s) group (Oldenwald 1986). *c)* Irwin (1994). *d)* Sharp (1990). *e)* Possible small group (Schneider et al. 1986), uncertain membership in Virgo Cluster (Chamaraux et al. 1980). *f)* Giuricin et al. (1990). *g)* Turner et al. (1988). *h)* Arp 303 (with IC 0563), possibly interacting (Surace et al. 1993), possible triple. *i)* Zaritsky et al. (1997).